

Digital flow platform for the synthesis of high-quality multi-material perovskites

Diego Iglesias,^a Christopher Tinajero,^a Simone Marchetti,^a Jaume Luis-Gómez,^b Raúl Martínez-Cuenca,^b Jose F. Fuentes-Ballesteros,^b Clara A. Aranda,^c Alejandro Martínez Serra,^d María C. Asensio^{e,f} Rafael Abargues,^d Pablo B. Boix,^g Marcileia Zanatta,^{a,h} Victor Sans^{*a}

^a Institute of Advanced Materials (INAM), Universitat Jaume I, Avda Sos Baynat s/n, 12071, Castellón, Spain

^b Department of Mechanical Engineering and Construction, Universitat Jaume I, 12071, Castellon, Spain

^c Center for Nanoscience and Sustainable Technologies (CNATS), Department of Physical, Chemical and Natural Systems, Universidad Pablo de Olavide, 41013, Seville, Spain

^d Instituto de Ciencia de los Materiales de la Universidad de Valencia (ICMUV), Valencia, 46980 Spain

^e Materials Science Institute of Madrid (ICMM/CSIC), Cantoblanco, E-28049 Madrid, Spain

^f MATINÉE, the CSIC Associated Unit between the Materials Science Institute (ICMUV) and the ICMM, Cantoblanco, E-28049 Madrid, Spain

^g Instituto de Tecnología Química, Universitat Politècnica València-Consejo Superior de Investigaciones Científicas, Av. dels Tarongers, València, 46022, Spain

^h Departament de Química Física i Analítica, Universitat Jaume I, Av. Sos Baynat s/n, 12071 Castelló de la Plana, Spain

**sans@uji.es*

Abstract:

Perovskite materials have demonstrated great potential for a wide range of optoelectronic applications due to their exceptional electronic and optical properties. However, synthesising high-quality perovskite films remains a significant challenge, often hindered by batch-wise processes that suffer from limited control over reaction conditions, scalability and reproducibility. In this study, we present a novel approach for synthesising single-crystal perovskites with an optimised continuous-flow reactor. Our methodology utilises a 3D printed system that enables precise control over reactant concentrations, reaction times, and temperature profiles. The reaction chamber was designed and optimised by combining residence time distribution (RTD) studies and computational fluid dynamics (CFD) simulations. High-quality single-crystal perovskites with different formulations were obtained employing seeding and seedless conditions. The possibility of synthesising mixed halide single crystal perovskites with different compositions along

its structure was demonstrated by simply shifting the feedstock solution during the crystallisation, demonstrating the versatility of this technology.

Keywords: Perovskites • continuous-flow • 3D printing • reactor design • digital process engineering

Highlights

- A digitally designed and additively manufactured crystallisation platform encompassing vision control, optimised heating and flow profiles for the production of perovskite single crystals is presented.
- Reactor modelling and computational fluid dynamics were employed to design flow reactors with optimal features for single-crystal perovskite reaction and crystallisation.
- High-quality single crystals were fabricated employing seeded and seedless crystallisation conditions.
- Multi-material compounds based on mixed halide perovskites with a compositional gradient along its longitudinal axis were created.

1. Introduction

Over the recent decade, the interest in hybrid organic-inorganic perovskites has greatly risen. Thanks to their widely tuneable semiconductive and optoelectronic properties, this family of materials has seen great developments in fields like solar cells,¹ X-ray sensors,² LEDs³ or memristors.⁴ Part of the interest is due to the possibility of their synthesis under mild conditions using solution-based approaches. Most of the applications using these materials employ polycrystalline thin films, but the boundaries between grains hinder the maximum performance of the resulting devices and can induce material degradation paths.⁵ In this regard, the use of monocrystalline perovskites offers superior properties in terms of lower trap density, longer carrier diffusion lengths, and resistance to degradation by moisture.⁶

Perovskite single crystals have been classically grown in batch with techniques like antisolvent crystallisation,⁷ solvent evaporation⁸ or solution temperature lowering.⁹ Achieving millimetre-sized crystals with these methods required days. In contrast, the inverse temperature crystallisation method (ITC), based on the retrograde solubility of the perovskite (solubility decreases as temperature is increased), allows it to grow crystals in a matter of hours.¹⁰ One of the main problems derived from its use is the loss of control over nucleation, as the increase in temperature also accelerates crystallisation kinetics, resulting in a decrease in crystal quality and reproducibility between experiments.¹¹ This is reflected in the range of electronic defect concentrations reported, even for the monocrystalline structures¹². Different strategies have been used to overcome these issues, including control over precursor quality,¹³ slow ramped heating of solution, use of

seeds¹⁴ or localised heating.¹⁵ Nevertheless, batch synthesis has limitations since the maximum crystal size is dependent on the volume and concentration of the starting solution, and the inhomogeneous distribution of temperature and precursor concentration within the crystallisation chamber might affect the quality of the crystals.

Continuous flow synthesis has become an important asset in the transition to more sustainable processes. In complex processes like crystallisation, the use of continuous flow reduces mass and heat transfer limitations, resulting in more homogeneous product distribution compared to batch, improving the overall reproducibility.^{16,17} In the field of perovskites, there are numerous reports of their application for the synthesis of crystalline materials, often upgrading the properties of their batch-synthesised counterparts.^{18,19} The synthesis of nanostructured perovskite materials is typically carried out in coil reactors with cross sections under 1 mm.²⁰ In the case of higher lateral area materials, like millimetre-sized monocrystalline perovskites, the cross-section of the tubing severely limits their growth. Meanwhile, as the cross-section increases, mass and heat transfer limitations present in batch might arise¹⁶. Therefore, there is a need for developing new geometries where crystals have sufficient space for their growth while maintaining the advantages of continuous flow.

Digital reactor design combines computer-aided design (CAD), computational fluid dynamics (CFD) and additive manufacturing to produce advanced reactors with tailored geometries and advanced mixing features.^{21,22} Modelled geometries can be used for simulating the resulting flow pattern with CFD, calculating parameters like flow streamlines, velocity and temperature fields, or tracer transport to validate the model. The analysis of CFD permits the detection of flow maldistributions (short-circuits, dead volumes, etc.) to optimise the CAD geometry.²³ Finally, thanks to 3D printing (3DP), validated reactors can be swiftly manufactured onsite for their experimental application.^{24,25} Another significant step towards highly controlled and reproducible synthetic platforms is the development of digital flow platforms. Reaction conditions can be transformed into digital inputs; therefore, solution delivery or reactor temperature can be controlled through an interface for setting up experiments. Additionally, the implementation of in-line analytics allows recording data, like absorbance²⁶ or photoluminescence,²⁷ for monitoring crystal growth in real-time. With this, variability caused by human intervention is minimised, and products obtained can be directly correlated with acquired data to better understand the process. It could even be possible to implement self-optimisation algorithms for achieving synthesis by selecting target properties directly.^{20,28,29} Digital flow platforms have been successfully used for the synthesis of crystalline materials,^{27,30,31} and very recently, the growth of high-quality perovskites has been monitored by employing in-situ video imaging.³² We presented in our previous work their potential in the synthesis of perovskite single crystals,¹⁹ albeit further developments were required to better control the number of crystals synthesised and to improve their quality.

Thanks to the flow platform developed during this work, we achieved a high degree of reproducibility, allowing for the synthesis of perovskite single crystals with consistent

properties and minimal batch-to-batch variations. Moreover, the continuous-flow approach offers improved reaction kinetics, leading to enhanced crystallinity, homogeneity and reduced defect density in the resulting perovskite films. We also investigate the impact of various reaction parameters, such as precursor flow rates, reaction temperatures, and solvent compositions, on the properties of the resulting films and device performance. Furthermore, we use the same platform for the synthesis of different perovskite materials, and its design enables the change of material without interrupting the process. XPS and X-ray diffraction (XRD) have confirmed that the successive perovskite films obtained are stoichiometrically and structurally homogeneous. Hence, our study demonstrates the successful synthesis of high-quality perovskite films under continuous-flow conditions, offering a scalable and reproducible method to produce perovskite-based optoelectronic devices. The continuous-flow approach presents an exciting avenue for advancing the field of perovskite research, enabling improved device performance and paving the way for large-scale commercialisation of perovskite-based technologies.

2. Results and discussion

2.1 Design of flow platform

The main aim of the work was to build a low-cost platform for consistently producing perovskite single crystals with improved properties. In this regard, a strategy addressing multiple fronts for controlling the crystallisation process was developed. As a starting point, we used the combination of flow and a 3D printed reactor to develop a system capable of yielding perovskite single crystals based on previous work.¹⁹ However, further developments of the technique were required to demonstrate an optimised control over the crystallisation processes. To achieve this, a platform was designed (Figure 1) with an optimised flow diffuser to generate a pattern for homogeneous precursor distribution in the crystallisation chamber. The localised homogeneous heating of the surface of the crystallisation chamber aimed to improve control over nucleation and crystallisation.

In parallel, the implementation of a vision control algorithm allows the monitoring of growth kinetics in real time. Finally, the implementation of flow control methodologies with multiple programmable pumps was developed to dynamically control the composition of the crystallisation environment, thus enabling the development of innovative single-crystal multi-materials.

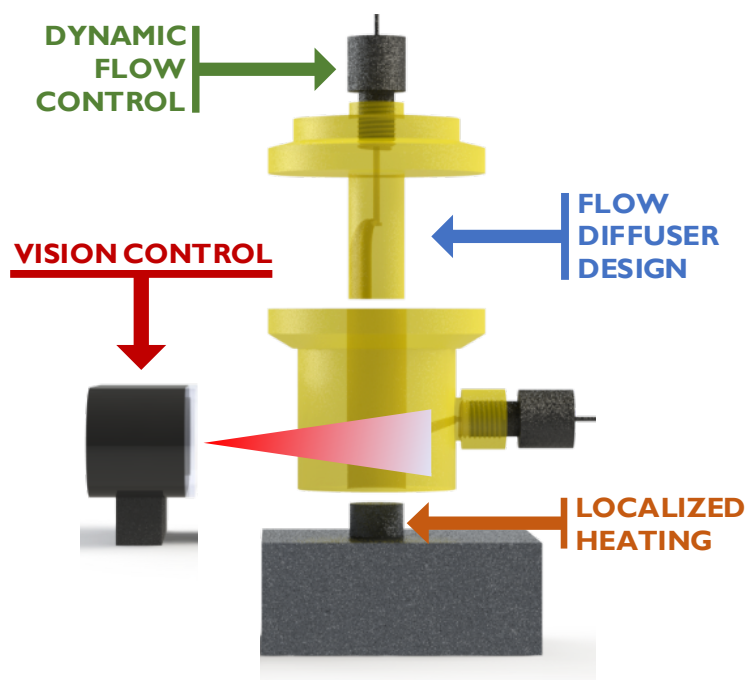


Figure 1. General overview of the digital flow platform developed in this work

The core reactor was designed as a two-bodied system, plus additional accessories for controlling flow, monitoring, and heating. The bottom part featured a 10.5 mm diameter circular hole for introducing glass substrates and an outlet to maintain steady state flow conditions. The top part was designed as a cylinder, featuring flow channels to act as an inlet, that was inserted into the reactor body. Once both parts were connected and the system closed using a clamp, a small chamber of 1.5 mm height was created to grow crystals with a volume of 0.13 mL (more detailed measurements can be seen in Figure S1). The pieces were manufactured using 3D printing techniques based on stereolithography, which is based on the focused polymerisation of a thin layer of ink inside the vat using a laser beam.³³ The photopolymerisable resin selected was High Temp Resin (HRT) from Formlabs, as we previously demonstrated its compatibility with conditions used for the Inverse Temperature Crystallisation (ITC) of the MAPbBr₃ perovskite.¹⁹

2.2 Optimised design based on flow dynamics

The first step was the study of the flow inlet configuration to achieve a more homogeneous flow distribution in the crystallisation chamber compared to the previous model of the designed reactor. In the original iteration, the flow diffuser, which includes the flow inlet and the diffuser, was designed as a cylinder featuring a flow line divided into seven channels to distribute the flow homogeneously into the reactor.¹⁹ Different flow diffusers for the reactor were fabricated with a varying number of holes and orientations relative to the reactor's lower outlet. An orienting arrow was added to the upper design to aid positioning, as shown in Figure 2A.

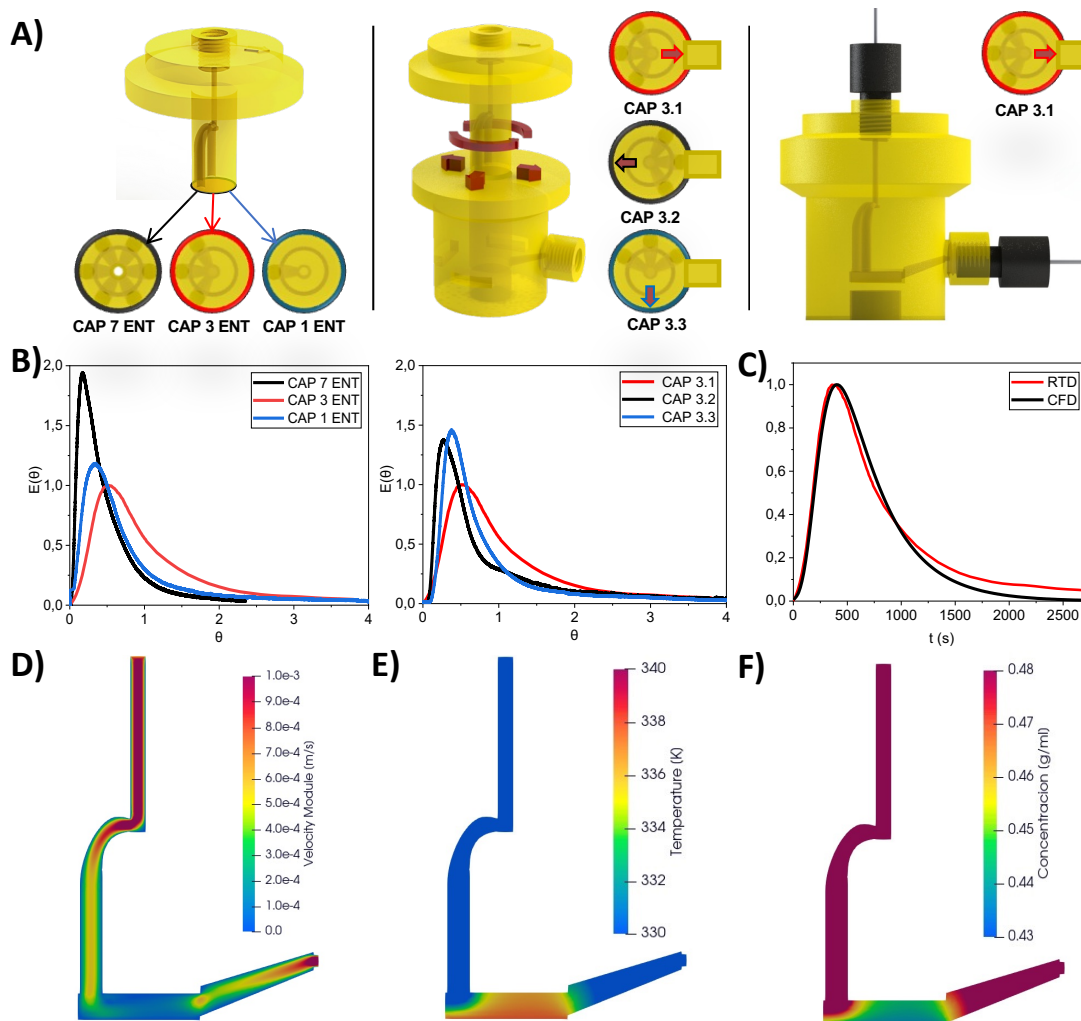


Figure 2. A) Flow diffuser development studied by residence time distribution (RTD) and CFD. B) Left: analyses of multiple inlet flow diffuser geometries. Right: geometry orientations are studied as a function of the angle between the inlet and outlet orientations. C) Comparison of RTD study and CFD simulation for the optimal flow diffuser geometry. CFD simulations of: D) velocity profile inside the reactor; E) temperature distribution field; F) solubility field of MAPbBr₃ in dimethylformamide (DMF).

To evaluate the impact of different flow diffuser configurations, pulse tracer-based residence time distribution (RTD) studies were conducted as a quantitative measure of the internal mixing within the reactor.^{31,34} Here, an inert tracer pulse was injected into the reactor, and the output was constantly recorded with a UV-VIS spectrophotometer. With this, the residence time distribution function ($E(\theta)$) can be calculated to evaluate differences in residence time of fluid particles. Figure 2B shows the $E(\theta)$ curves of the different geometries studied. Initially, the number of inlets in the reactor's flow diffuser was evaluated (1, 3, 7 inlets), all oriented in an initial 180° configuration to the outlet, using a liquid flow rate of 50 $\mu\text{L min}^{-1}$. The curve corresponding to the flow diffuser with three inlets, referred to as CAP 3 ENT, presents a distribution closer to the ideal normalised distribution time of 1, while the other two show premature tracer breakthrough, suggesting issues such as channelling or short-circuiting.

Once it was established that the configuration with three inlets (CAP 3 ENT) offers better flow distribution compared to the 1 and 7 inlet designs, the orientation of the inlets was

studied. The orientation CAP 3.1, in which the three inlets of the reactor's upper part are situated opposite the outlet, showed a more homogeneous flow distribution compared to the other inlet angles studied, which showed a less homogeneous tracer concentration. To validate these results, a CFD simulation of the system was performed. As shown in Figure 2C, an overall agreement between the RTD experimental curve and validated the CFD simulations performed. The experimental curve experiences a slightly longer tail associated with wall effects and inhomogeneities of the structured reactor.

The heating system was designed to provide heat specifically directed towards the crystallisation surface, thus avoiding undesired secondary nucleation and crystal growth. An aluminium block connected to a heating resistance controlled by a PID (Proportional-Integral-Derivative) temperature controller was fabricated featuring a little pivot connected with the cavity of the bottom part of the main body of the reactor. A thin wall of 1.8 mm separated the glass substrate and the heating block pivot. The rest of the reactor and heating block were adequately insulated from the environment using thick polymer walls. A calibration of the relationship between the nominal temperature of the PID controller and the inside of the chamber was performed (Figure S2).

The flow and temperature gradients within the crystallisation chamber play a key role in the uniformity of the perovskite concentration and uniformity during the crystallisation process. Therefore, using the values previously validated at the RTD, heat exchange and velocity profiles at the interior of the crystallisation chamber were modelled using CFD. A flow of precursor solution through the reactor passing through the crystallization chamber was simulated while simultaneously, the bottom section of the reactor was constantly heated. In Figure 2D, it can be noticed that the orientation of the inlets promotes a smooth transition from high to low velocities, allowing the solution to homogenise near the bottom where crystallisation starts occurring, also promoting steady, regular crystal growth. Regarding temperature, the contour in Figure 2E shows the formation of a steady gradient of temperature in the chamber that decreases with the distance to the heating wall, as expected. Also, it can be noticed the effect due to the entrance of the cold stream at the rear part of the chamber. The temperature increases as the flow advances through the chamber, promoting nucleation in the middle/frontal region of the reactor. This temperature distribution (T) has a direct effect on the solubility concentration (C) of MAPbBr₃ in dimethylformamide (DMF) (Eq. 1).¹⁴

$$C = 0.0023 \times \exp\left(\frac{1782}{T+273.15}\right) \quad (1)$$

Figure 2F clearly shows that lower solubilities are observed at the bottom of the reactor, suggesting that saturation will occur in this area, leading to crystal nucleation near the bottom. Additionally, even if some nucleation occurs near the chamber entrance, significant crystal growth is unlikely due to the higher solubility in that region.

2.3 Vision control of growth kinetics of perovskite single crystals

Once the optimal reactor configuration was selected, the platform was ready for the growth of perovskite single crystals. MAPbBr₃ was used as the case model, as we

previously demonstrated the possibility of its growth using continuous flow and the ITC method.¹⁹ The monitoring was conducted using the setup illustrated in Figure 3A. The system features a 3D-printed platform that supports the heating block of the crystalliser, along with two perpendicular mounts that house cameras. These cameras capture images at specified time intervals, which are subsequently processed using the OpenCV library³⁵ for image recognition and Python scripts for data analysis. The reactor is equipped with two 33mm² rectangular windows, perpendicular to the substrate, that allow for the observation of perovskite crystal growth. During the analysis, the crystal size is normalised using these windows as a reference, ensuring precise and consistent measurement of crystal growth. The analysis software developed for this purpose is available on a supplementary GitHub repository.³⁶ The methodology was validated by conducting analyses of the vision computing area (VCA), comparing them to the experimental determination of the size of the perovskites, which was measured outside the crystallisation chamber with a calliper. A good experimental correlation was found (Figure 3A). It is important to mention that a negative x0 indicates that the VCA system cannot reliably measure very small perovskites (<1 mm²). Hence, the system can assess the growth of perovskites, yet the nucleation processes can only be qualitatively evaluated.

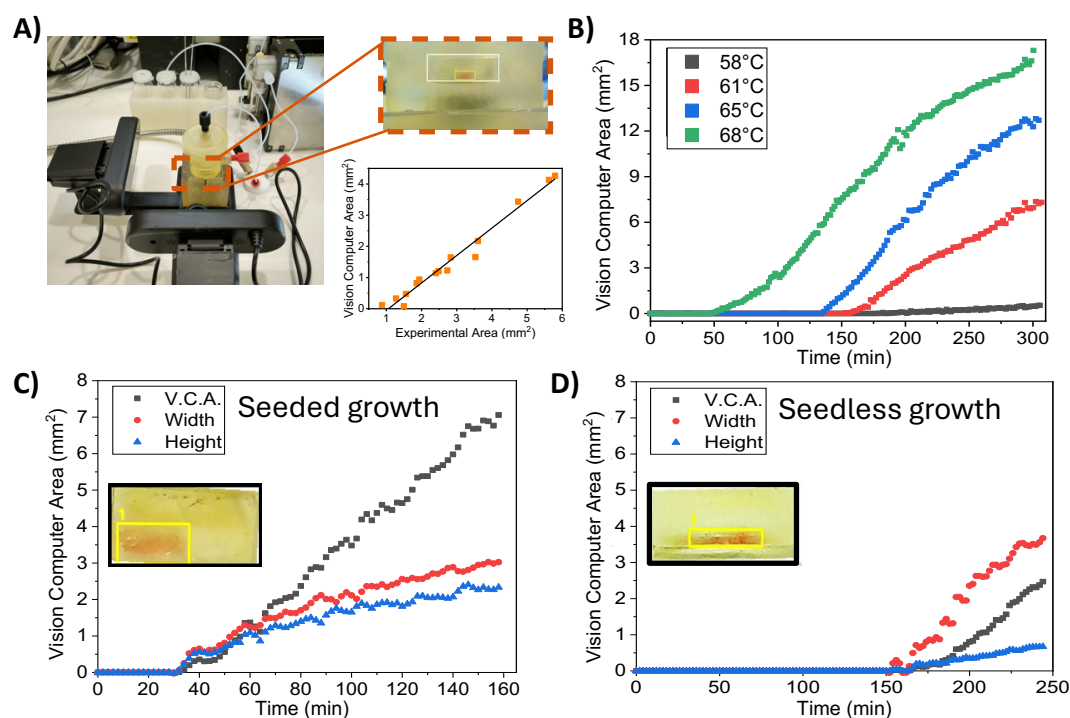


Figure 3. A) Control setup of the growth of perovskite single crystals. The correlation between the vision computing area (VCA) and the experimental area of the perovskites was $y = -0.93 + 0.88x$. $R^2 = 0.976$. B) Temperature-dependent perovskite growth kinetics for unseeded perovskites. Crystallisation kinetics for C) seeded growth crystals; D) unseeded growth crystals.

A series of experiments were conducted to monitor the growth of MAPbBr₃ perovskite single crystals under varying conditions. The concentration of reagents (methylammonium bromide and lead (II) bromide in dimethyl formamide) remained

constant at 1.2 mol L^{-1} , while other parameters were systematically varied. Initially, experiments were conducted without the use of seed crystals, focusing on evaluating the influence of key parameters such as flow rate and temperature on single crystal growth. Growth temperatures were kept as low as possible to minimise the apparition of secondary crystal nuclei while enabling stable crystal growth. A summary of the experimental conditions is provided in Table S1, while Figure 3B illustrates the differences in growth kinetics for different temperatures under the same conditions. The crystal growth kinetics presented a direct dependence on the solution temperature. At $58 \text{ }^\circ\text{C}$, no nucleation was observed until 200 minutes, followed by slow growth. Alternatively, by selecting a temperature of $68 \text{ }^\circ\text{C}$, nucleation started at 50 minutes, and the slope was notably more pronounced. This behaviour was expected since, at higher temperatures, it's easier for an oversaturated system to overcome the nucleation energy for the subsequent formation of nuclei, and the growth kinetics are also favoured at higher temperatures.¹¹

While nucleation time decreases at higher temperatures, the probability of uncontrolled nucleation increases. Seed-assisted growth is a way to enable growth at lower temperatures. Here, previously grown and harvested MAPbBr_3 single crystals are introduced into the saturated solution to be used as nucleation centres for further growth. For the case of a 1.2 mol L^{-1} MAPbBr_3 precursor solution at a $61 \text{ }^\circ\text{C}$ temperature, with a $25 \text{ } \mu\text{l min}^{-1}$ flowrate, seeded and unseeded experiments were monitored (figures 3C and 3D). Seeded experiments presented a 30-minute induction time where growth was not observed. On the other hand, non-seeded experiments typically present a time of approximately 150 minutes of induction time before crystals are observed. At selected conditions, the solution presents a low supersaturation level. Hence, further nucleation is unlikely,¹¹ thus inhibiting the appearance of secondary crystals. However, this makes seedless growth challenging. Another difference observed is the aspect ratio of crystals, as also seen in Figure 3C. Seeded crystals present more similar growth speeds in both horizontal and horizontal directions, while unseeded crystals favour horizontal growth (Figure 3D), resulting in a higher area-to-thickness ratio. It should be considered that partial redissolution of the seed during the initial minutes increased the supersaturation level in all the surroundings of the crystal. This would cause an acceleration of growth in all directions, as observed in Figure 3C. Alternatively, in seedless experiments, crystals remained thinner, possibly due to a combination of factors that need further exploration, like the temperature difference between the top and bottom, or the effect of the flow parallel to the crystal surface.

Additionally, the platform was tested for the synthesis of MAPbCl_3 crystals, as it also presented retrograde solubility when precursors were dissolved into a mixture of dimethyl formamide and dimethyl sulfoxide (1:1). In this case, different solution concentrations were tested at the same conditions used for the previous bromide experiments (61°C and $25 \mu\text{L min}^{-1}$ flowrate). MAPbCl_3 crystals were obtained successfully using a 0.8M solution concentration, demonstrating the possibility of extending the principles of the platform to other systems that can be grown via ITC of the platform. However, MAPbCl_3 appeared to be more prone to secondary nucleation, something that can be controlled by a more exhaustive adjustment of crystallisation conditions. Moreover, due to the

colourless look of the crystals, growth could not be monitored by the existing setup. Further developments of the platform could implement photoluminescence measurements or other methodologies for overcoming this issue.

2.4 Characterisation of perovskite single crystals

Selected crystals synthesised with the previously discussed methodology were characterised to evaluate their properties. Seedless-grown crystals showed a clear and homogenous structure, as seen in Figure 4A, with no observable morphological defects, while seeded crystals presented a comparable appearance but with the initial seed embedded in the centre. The XRD spectra (Figure 4B) showed diffraction peaks at 14.97° , 30.14° and 45.90° , which can be attributed to the (100), (200), and (300) facets, confirming the growth of the monocrystalline cubic MAPbBr₃ perovskite.³⁷ Atomic force microscopy of the crystal revealed a surface roughness of 2.93 nm for the seedless-grown crystal and 1.46 nm for the seeded crystal (Figure S3), greatly improving the surface smoothness compared to the literature.¹⁹

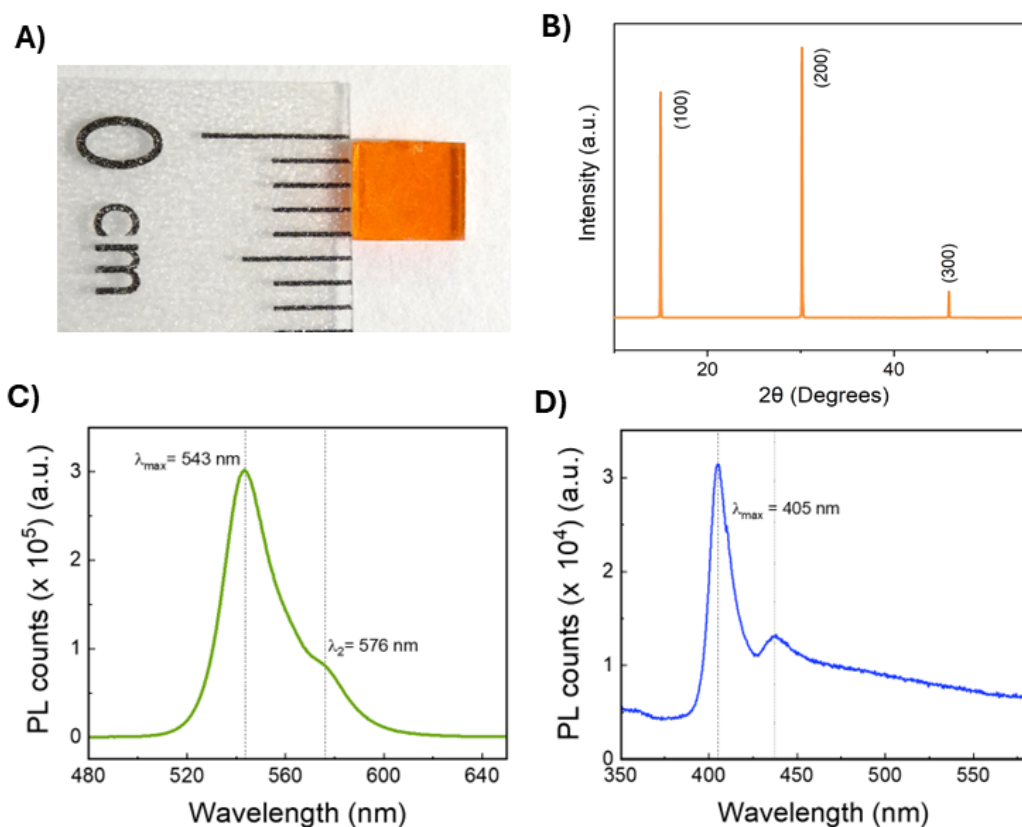


Figure 4. A) Image of a seedless synthesised MAPbBr₃ single crystal. B) X-ray diffraction spectra of the seedless-grown MAPbBr₃ crystal. C) B) X-ray diffraction spectra of the seedless-grown MAPbBr₃ crystal. D) Photoluminescence measurements of a seed containing MAPbCl₃ single crystal.

The photoluminescence (PL) properties of the seedless crystals were also evaluated (Figure 4C). Crystal presented an intense peak at 543 nm, corresponding to MAPbBr₃ perovskite. A minor secondary peak can be observed at 576 nm, which may be due to

reabsorption phenomena observed in monocrystalline materials.³⁸ Time-resolved photoluminescence (TRPL) decay revealed a τ_F of 181.7 ns (figure S4A), shorter than the values we observed in the previous iteration of the platform.¹⁹ Crystals grown using an initial seed presented higher photoluminescence intensity and a less pronounced shoulder, which indicates lower defect concentration. Interestingly, τ_F was noticeably shorter, with a value of 91.3 ns. It has been reported that the shortening of photoluminescence decay can be related to an increase in crystallinity quality and decreased surface roughness in bulk single crystals.³⁹ However, there are also reports about how this is linked to a decrease in photoluminescence intensity, as surface defects play a key role in PL emission. Paradoxically, crystals grown in flow with the seed-assisted method presented shorter decay times but higher emission intensity. It can be considered that flow might have a further influence on crystal morphology and their properties, but the complexity of the underlying mechanisms would require extensive exploration. In the case of MAPbCl₃ crystals, the maximum PL intensity peak is expected at 405 nm. However, a secondary peak at 440 nm can also be observed (Figure 4D), and, compared to MAPbBr₃, it presents a higher relative intensity compared to the main peak. This corroborated that further optimisation of the conditions of the chloride crystals would be required to yield optimal PL properties.

Growth of mixed halide perovskite single crystals

The possibility to adjust the flow rate and composition by employing multiple pumps during the experiment enables the dynamic modification of the crystallization conditions. This is a clear advantage over conventional batch processes, where a change of solution requires stopping the process and the transfer of the crystal to another vessel or diluting the mother liquor by the addition of a new substrate solution. These actions inevitably disturb the growth, as crystals might redissolve partially until supersaturation temperature is reached again, and the manipulation of the crystal might generate surface-level irregularities. In that sense, the use of multiple pumps allows the introduction of different solutions without manipulating the reactor, making this transition smoother. Hence, novel single-crystal multi-materials can be generated with this approach. As a proof of concept, a mixed halide methylammonium lead-based perovskite was synthesised.

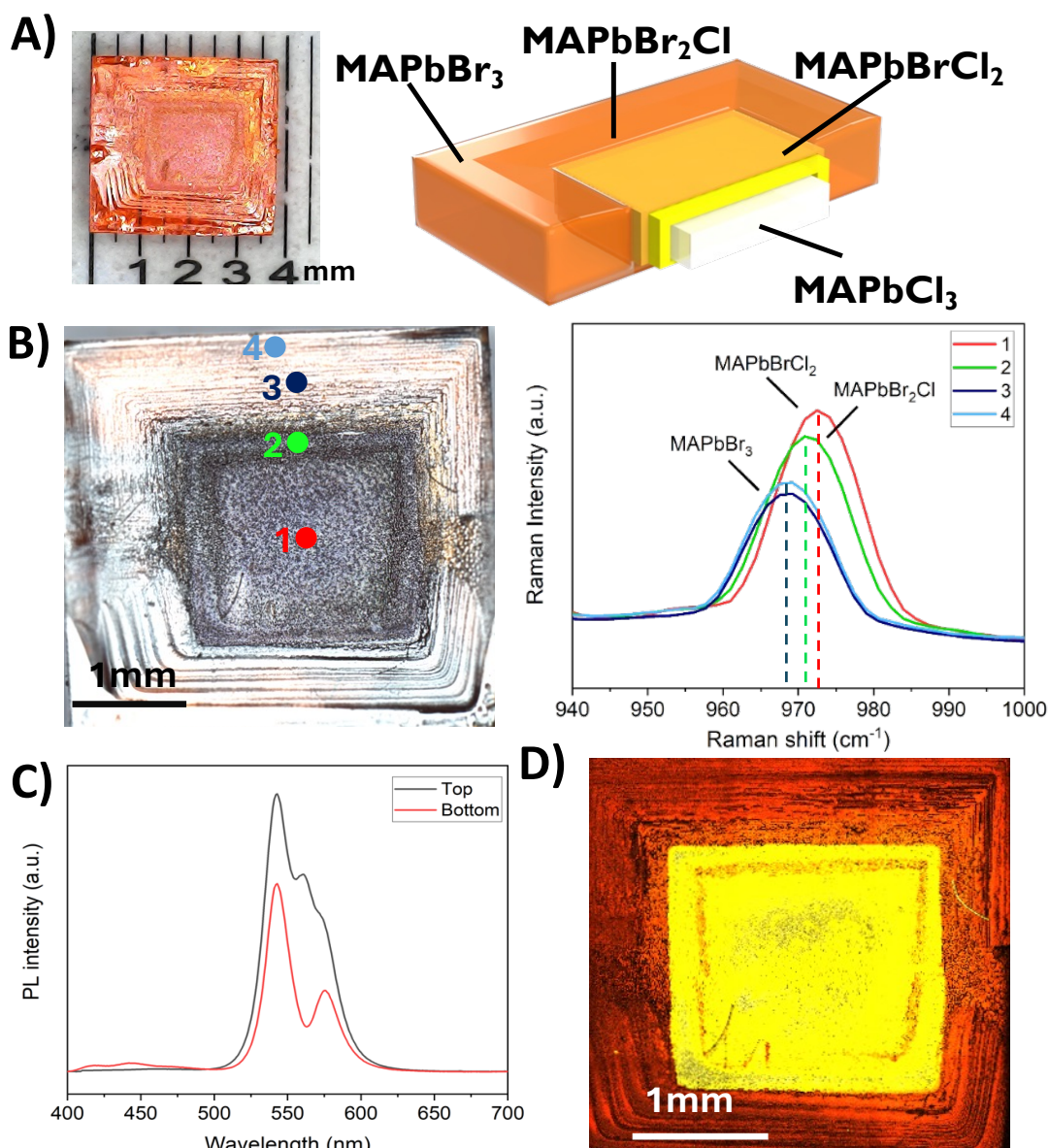


Figure 5. A) Picture of a mixed halides perovskite single crystal and diagram of crystal composition B) Raman shift spectra of selected points. C) Photoluminescence of crystal faces D) Confocal photoluminescence microscope picture of the mixed composition perovskite single crystal.

Selected materials for the experiments were MAPbCl_3 and MAPbBr_3 , as they share a cubic structure with the same space group⁴⁰ and they were both successfully synthesised in the reactor. The first step was the seed-based growth of a crystal of MAPbCl_3 using 0.8 M solution of precursors in a mixture of DMF and dimethylsulfoxide (DMSO) (1:1 (v:v)) at 65°C with a flow rate of 25 $\mu\text{L min}^{-1}$ since we already used these conditions successfully. After a selected growth time of 2 h, a step change of feedstock solution to a 1.2 mol L^{-1} of precursors in DMF was performed with a second programmable pump, maintaining the overall flow rate constant at 25 $\mu\text{L min}^{-1}$. Growth of the coloured bromide containing perovskite was constantly monitored with the vision computing platform (Figure S5). The resulting crystals (Figure 5A) are multi-component, with a clear colour gradient across the surface. The crystals were not flat on the surface, they presented a trapezoidal shape, presumably due to the bigger lattice structure of Br-containing crystals

versus the smaller Cl-containing ones. It is noteworthy that growth experiments in reverse order, starting from a MAPbBr₃ and then introducing MAPbCl₃ solution, were not possible, as the crystal was swiftly dissolved once the solution reached the inside of the crystallisation chamber. MAPbCl₃ growth requires a DMF/DMSO 1:1 solution, but MAPbBr₃ shows very small retrograde solubility in DMSO, and its solubility is over ten times higher at selected conditions⁴¹. Thereby, the continuous growth of multiple material single crystals requires a thorough revision of the solvent compatibility for each step.

Raman spectroscopy was employed to probe the composition of the crystal at different points (Figure 5B). The C-N stretching Raman band of the methylammonium (MA) varies as a function of the halide of the corresponding perovskite in the series MAPbCl_xBr_y.⁴⁰ In Figure 5, point 1 was measured in the centre of the crystal at 5 μm depth (Figure S6), showing a Raman shift of 977 cm⁻¹ (MAPbCl₃). However, at the same point, but at the surface, the Raman shift observed was 974 cm⁻¹ (MAPbCl₂Br), thus indicating a compositional from the initial MAPbCl₃ perovskite. Furthermore, point 2 at the surface showed a Raman shift of 971 cm⁻¹ (MAPbClBr₂) Points 3 and 4 clearly correlate to the growth of the crystal under predominantly PbBr₂ stock solution. Here, a Raman shift of 968 cm⁻¹ confirmed the presence of MAPbBr₃ on the surface of the crystal. Interestingly, X-ray photoelectron spectroscopy (XPS) probed at similar points than shown in Figure 5B showed that on the surface (1-10 nm) were bands consistent with MAPbBr₃, showing no detectable signals of chlorine (Figures S7 and S8). The core levels of Pb, C, Br, N, and O confirm the spectroscopic homogeneity of the top perovskite film, MAPbBr₃.

The photoluminescence properties of the crystal were recorded and a difference in behaviour between the two faces was observed (Figures 5C and S9, Table S3). Both faces presented a maximum emission at 543 nm, attributed to MAPbBr₃, but then different secondary peaks appeared. The 560 nm and 576 nm correspond, presumably, to reabsorption processes, and are more noticeable in the top layer, where they might be related to the height differences observed in the surface. On the other hand, the contribution of MAPbCl₃ can be detected in the bottom layer at 418 and 443 nm, where MAPbBr₃ growth was restricted due to physical limitations of space. To give further insight into this observation, confocal photoluminescence microscopy images were taken, with selected wavelengths to detect the perovskites studied (Table S4). Figure 5D reveals an outer shell of MAPbBr₃, that corresponds to the transparent orange sections (Figure 5A). Meanwhile, the central section of the crystal features different species that have mixed halide compositions. There is a gradient where proximity to the core of the crystal corresponds to lower wavelengths, signalling species with increasing proportions of chloride. This indicated the growth of perovskite layer by layer with a gradual change of compositions, as the initial medium containing chloride solution is replaced by the bromide.

Interestingly, MAPbBr₃ preferentially grew in the horizontal direction, towards the outer edges of the crystal, while it did not cover the central area for the top layers. Also, bromide ion has a higher radius than chloride, therefore as bromide content is increased cell size

presents higher values. The combination of these factors could explain the observed difference in behaviour between faces, and the height difference existing between the inner and outer areas (Figure S10).

3. Conclusions

The development of a novel digital flow platform for the controlled synthesis of perovskite single crystals enables the fabrication of advanced high-quality materials in a controlled and reproducible fashion. The optimisation of the heating chamber and flow conditions offered enhances control over the temperature profile within the crystallisation chamber and offers great potential for future scaling up of the process. Vision control can help in the understanding of growth kinetics, allowing a better selection of reaction conditions.

Single crystals with improved surface smoothness were generated with this platform employing seeded and interestingly highly challenging unseeded conditions. The capabilities of the digital and programmable platform were demonstrated by synthesizing novel single-crystal perovskites as individual highly stoichiometric films, even at thicknesses of just a few nanometres. These films could exhibit various halide compositions (MAPbCl₃, MAPbBrCl₂, MAPbBr₂Cl, and MAPbBr₃), by simply dynamically switching the precursor solution during a single-crystal growth experiment. A total of four different perovskites were integrated into a single crystal material, thus opening the possibility to the discovery of new materials, especially new combinations of multi-material single-crystal perovskites with advanced optoelectronic properties.

Methodology

Materials. CH₃NH₃Br (>99 wt%) and CH₃NH₃Cl (>99 wt%) were purchased from Great Cell Solar Materials. PbBr₂ (>98 wt%), PbCl₂ (>98 wt %), DMF (> 99.8 wt%, anhydrous) and DMSO (> 99.9 wt%, anhydrous) were purchased from Merck. Salts and solvents were used as received without any further purification.

Precursor solution preparation. In the typical synthesis used for this work, 1.34 g of CH₃NH₃Br (>99 wt%, Great Cell Solar Materials) and 4.404 g of PbBr₂ (>98 wt%, Merck) were dissolved at 1:1 molar ratio in 10 mL of DMF (>99.8 wt%, anhydrous, Merck) under nitrogen atmosphere to produce a 1.2 mol L⁻¹ solution of MAPbBr₃ and 0.54 g of CH₃NH₃Cl (>99 wt%, Great Cell Solar Materials) and 2.22 g of PbCl₂ (>98 wt %, Merck) were dissolved at 1:1 molar ratio in 5 mL of DMF (>99.8 wt%, anhydrous, Merck) and in 5 mL of DMSO (> 99.9 wt %, anhydrous, Merck) under nitrogen atmosphere to produce a 0.8 mol L⁻¹ solution of MAPbCl₃. Solutions were kept at room temperature under stirring and filtered before starting the crystallisation with 0.2 μm pore size PTFE filter.

3D printed reactor production. The reactor was modelled using Solidworks CAD software and converted to standard tessellation language (STL) format. It was printed using a Formlabs 3 low-force stereolithography printer loaded with off-the-self Formlabs High Temp resin. STL files were sliced using Formlabs slicing software, Preform, and

printed with a layer height of 50 μm using the settings recommended by the manufacturer. EPDM O-rings were purchased from RTC Couplings. Clamps were purchased from Leybold.

Heat and temperature control. A homemade setup consisting of a PID temperature controller connected to a cartridge heater was produced. The cartridge was introduced into a bespoke aluminum block and its temperature was monitored by a thermocouple connected to the PID temperature controller. The temperature at the base of the crystallisation chamber was measured with a high-resolution contact thermometer after waiting for two hours. A calibration for the correlation between temperature of the block and temperature at the surface of the crystallisation chamber was done (Equation S1).

RTD studies. The experimental procedure utilized a setup consisting of two syringe pumps: one for controlling the primary flow rate and the other for loading a 50 μL loop into an automated 6-way Rheodyne valve. This valve facilitated the injection of a tracer pulse into the flow stream, simplifying the process. The valve was connected to a commercial flow cell, allowing a light beam to pass through and be detected by a UV-visible spectrometer operating at a fixed wavelength. All components were connected using 1/16-inch PEEK capillary tubing. The experiments were conducted with isopropanol as the solvent and a Methyl Red tracer solution (1 mg/L) in the same solvent, with a flow rate of 50 $\mu\text{L}/\text{min}$. The change in tracer concentration over time was monitored by measuring the absorbance peak at 525 nm in the UV-VIS spectra.

CFD studies. The CFD validation for the RTD was performed using OpenFOAM 2112. The 3D geometry was meshed using snappyHexMesh to obtain a mostly tetrahedral non-deformed mesh composed by 400k nodes. The simpleFoam solver was employed to obtain the steady state resolution of the flow in similar conditions to the RTD study with a flowrate of 50 mL min^{-1} . The fluid was considered Newtonian and incompressible (kinematic viscosity of $4.9 \times 10^{-6} \text{ m}^2 \text{ s}^{-1}$ and base density of 1425 kg m^{-3}) while the temperature was set to 20 $^{\circ}\text{C}$ (heating plate was off in this case). Then, a laminar transient simulation with frozen hydrodynamics was performed by using the scalarTransportFoam solver with a kinematic diffusivity of $10^{-8} \text{ m}^2 \text{ s}^{-1}$. The tracer pulse was injected with a concentration of 1 mg L^{-1} during 60 s and its evolution was solved over 2700 s.

CFD simulations for the heat transfer analysis were performed employing the chtMultiRegionSimpleFoam solver from OpenFOAM 2112, in addition to the conditions previously described for the RTD curve validation. Inlet flow was fixed at a temperature of 20 $^{\circ}\text{C}$, while the bottom area of the reactor was fixed at 65 $^{\circ}\text{C}$ (this temperature was determined from the steady-state temperature of the heating plate). Reactor walls were modelled with an experimentally determined thermal conductivity coefficient of $0.282 \text{ kg m s}^{-3} \text{ K}^{-1}$, while external temperature was set at 20 $^{\circ}\text{C}$ to model the heat exchange with the surrounding air in the room.

XPS studies. High-energy resolution X-ray photoelectron spectroscopy (XPS) measurements were conducted using a SPECS GmbH system, with a base pressure of 1.0×10^{-10} mbar. The system featured a PHOIBOS 150 2D CMOS hemispherical analyzer.

Photoelectrons were excited using the Al-K α line (1486.7 eV). Measurements were performed at room temperature with a pass energy of 20 eV. For all HR-XPS measurements, the samples were placed under ultrahigh vacuum (UHV) conditions, with the analysis chamber achieving a base pressure lower than 1.0×10^{-10} mbar.

Continuous-Flow single and multimaterial crystal growth experiments.

Continuous-flow single crystal growth experiments were conducted using two programmable Tricontinent C3000 pumps, each equipped with a 5 mL syringe. These pumps operated in sequence to maintain a continuous flow of the previously prepared precursor solution into the reactor. The pumps were controlled via an interface developed in Visual Studio with Python scripts. The reactor's internal temperature was adjusted between 58 °C and 68 °C and the flow rate between 12 $\mu\text{L min}^{-1}$ and 50 $\mu\text{L min}^{-1}$ for the experiments.

Multi-material crystal growth experiments were conducted similarly to the previous ones, with one key modification: each of the two pumps introduced a different solution, with the first pump delivering a 0.8 M solution of MAPbCl₃ in DMF/DMSO 1:1, followed by the second pump, which delivered a 1.2 M solution of MAPbBr₃ in DMF.

The procedure was similar to the previous one, with Continuous-flow growth experiments were conducted using two programmable Tricontinent C3000 pumps, each equipped with a 5 mL syringe. These pumps operated in sequence to maintain a continuous flow of different solutions into the reactor. The first pump pumping a solution of 0.8M MAPbCl₃ in DMF/DMSO 1:1 v:v, followed by the second pump, which delivered a 1.2 M MAPbBr₃ solution in DMF. The pumps were controlled via an interface developed in Visual Studio with Python scripts. The reactor's internal temperature was kept constant at 67 °C, and the flow rate was adjusted between 6 $\mu\text{L min}^{-1}$ and 25 $\mu\text{L min}^{-1}$ for the experiments.

Vision control of growth kinetics of perovskite single crystals

For the monitoring and analysis of perovskite crystal growth in continuous flow, a specialised algorithm was developed in Python, utilizing the OpenCV library for image processing. This algorithm facilitates automated and precise analysis of the images captured from the reactor during the experiments.

The camera system captures images of the reactor at predetermined time intervals, which are automatically loaded for processing. A Region of Interest (ROI) is defined in each image using a polygon with predefined coordinates, delineating the area where perovskite crystal growth is expected to be observed. This polygon is superimposed on the image to facilitate visualisation and analysis of the target area.

The images, originally in BGR format, are converted to the HSV (Hue, Saturation, Value) colour space to improve colour segmentation, thereby aiding in the identification of perovskite crystals. In this case, a specific colour range in the orange spectrum is used to detect lead perovskite. This colour range can be adjusted according to experimental needs, allowing for flexible adaptation to different lighting conditions or variations in sample composition.

Once the regions of interest are segmented based on colour, contours within these regions are detected. Each contour is analysed to determine its area, with those below a predefined threshold being discarded to avoid noise or irrelevant elements. Valid contours are highlighted in the original image to facilitate visual review.

The total area of the crystals detected within the ROI is calculated and stored for subsequent analysis. These area values are normalised based on the known size of the ROI, enabling accurate comparisons over time. Each area measurement is associated with the corresponding image capture time, creating a time series of data.

To improve data interpretation, a smoothing technique using a moving average with a three-point window is applied, reducing variability and highlighting trends in crystal growth. The results are presented in a graph showing the detected area over time, which is saved as a PDF for documentation. Additionally, the processed images are stored in a specific folder for further review.

This automated approach allows for continuous and detailed monitoring of perovskite crystal growth, providing valuable data for process optimisation and scientific research.

Characterisation

XRD spectra was measured in a Bruker D8-Advance diffractometer. CuK α radiation ($\lambda = 1.5406 \text{ \AA}$) was used for the direct recording of the signal by mounting the crystal in a sample holder.

Atomic force microscopy images were made using JSPM-5200 Scanning Probe Microscope from Jeol. Images were taken in contact mode for an area of $2 \times 2 \mu\text{m}$ with a pixel resolution of 256×256 .

PL and TRPL measurements were performed with the use of Edinburgh Instrument FLS 1000 fluorimeter with a picosecond pulsed diode laser EPL 375 nm as the excitation source. The pulse period was settled at 200 ns for steady-state PL and increased up to 500 ns for the TRPL performance with a time scale of 500 ns.

Raman spectra measurements were performed using a WITec Apyron confocal Raman microscope. A 785nm laser with a laser power of 9.62mW was used as excitation source with a Zeiss EC Epiplan-Neofluar Dic 100x objective.

Confocal fluorescence pictures were taken using a Leica TCS SP8 microscope using a 405nm laser as excitation source. Photoluminescence was acquired by using a series of PMT detectors with wavelength ranges described in Table S2, with a $53.1 \mu\text{m}$ pinhole and a Leica HC PL APO x10 objective.

CONFLICTS OF INTEREST

There are no conflicts to declare.

ACKNOWLEDGMENTS

This work has been funded by the project (PID2020-119628RB-C33, PID2020-119628RB-C32 and PID2020-119628RB-C31), MCIN/AEI/10.13039/501100011033. CT thanks the Generalitat Valenciana (CIGRIS/2021/075) for funding. The authors are grateful to the SCIC of the Universitat Jaume I for technical support. J. L-G. is supported by FPU21/03740 doctoral grant from the Spanish Ministry of Universities. CAA thanks the Spanish Ministry of Science and Innovation under contract number (TED2021-129758B-C33) MCIN/AEI/10.13039/501100011033/European Union NextGeneration EU/PRTR provided gratefully acknowledged financial support. MZ thank the funding received from “la Caixa” Foundation (ID 100010434) under the fellowship number LCF/BQ/PR24/12050016.

Author Contributions: Conceptualisation VS; Methodology VS, MZ, RAB, PB; Software Programming CT, J.L-G.; Validation DI, SM, JMX; Formal analysis DI, CT, VS; Investigation DI, SM, CAA, AMS, MCA; Resources; Data Curation DI, SM, MZ; Writing - Original Draft DI, MZ, CT; Writing - Review & Editing All authors; Visualisation; Supervision VS, MZ, RMC; Project administration VS; Funding acquisition VS, PB, RAB, MCA.

References

- 1 Alsalloum, A. Y. *et al.* 22.8%-Efficient single-crystal mixed-cation inverted perovskite solar cells with a near-optimal bandgap. *Energy & Environmental Science* **14**, 2263-2268 (2021). <https://doi.org:10.1039/D0EE03839C>
- 2 Wei, H. *et al.* Sensitive X-ray detectors made of methylammonium lead tribromide perovskite single crystals. *Nature Photonics* **10**, 333-339 (2016). <https://doi.org:10.1038/nphoton.2016.41>
- 3 Nguyen, V.-C., Katsuki, H., Sasaki, F. & Yanagi, H. Single-crystal perovskite CH₃NH₃PbBr₃ prepared by cast capping method for light-emitting diodes. *Japanese Journal of Applied Physics* **57**, 04FL10 (2018). <https://doi.org:10.7567/JJAP.57.04FL10>
- 4 Fernandez-Guillen, I. *et al.* Perovskite Thin Single Crystal for a High Performance and Long Endurance Memristor. *Advanced Electronic Materials* **10**, 2300475 (2024). <https://doi.org:https://doi.org/10.1002/aelm.202300475>
- 5 Liu, Y., Yang, Z. & Liu, S. Recent Progress in Single-Crystalline Perovskite Research Including Crystal Preparation, Property Evaluation, and Applications. *Advanced Science* **5**, 1700471 (2018). <https://doi.org:https://doi.org/10.1002/advs.201700471>
- 6 Wang, Q. *et al.* Scaling behavior of moisture-induced grain degradation in polycrystalline hybrid perovskite thin films. *Energy & Environmental Science* **10**, 516-522 (2017). <https://doi.org:10.1039/C6EE02941H>
- 7 Shi, D. *et al.* Low trap-state density and long carrier diffusion in organolead trihalide perovskite single crystals. *Science* **347**, 519-522 (2015). <https://doi.org:doi:10.1126/science.aaa2725>

- 8 Gu, Z., Huang, Z., Li, C., Li, M. & Song, Y. A general printing approach for
scalable growth of perovskite single-crystal films. *Science Advances* **4**, eaat2390
(2018). <https://doi.org/doi:10.1126/sciadv.aat2390>
- 9 Lian, Z. *et al.* Perovskite CH₃NH₃PbI₃(Cl) Single Crystals: Rapid Solution
Growth, Unparalleled Crystalline Quality, and Low Trap Density toward 108 cm⁻³.
Journal of the American Chemical Society **138**, 9409-9412 (2016).
<https://doi.org:10.1021/jacs.6b05683>
- 10 Saidaminov, M. I., Abdelhady, A. L., Maculan, G. & Bakr, O. M. Retrograde
solubility of formamidinium and methylammonium lead halide perovskites
enabling rapid single crystal growth. *Chemical Communications* **51**, 17658-17661
(2015). <https://doi.org:10.1039/C5CC06916E>
- 11 Zia, W. *et al.* Impact of Low-Temperature Seed-Assisted Growth on the Structural
and Optoelectronic Properties of MAPbBr₃ Single Crystals. *Chemistry of
Materials* **35**, 5458-5467 (2023). <https://doi.org:10.1021/acs.chemmater.3c00780>
- 12 Kumar, S., Hodes, G. & Cahen, D. Defects in halide perovskites: The lattice as a
boojum? *MRS Bulletin* **45**, 478-484 (2020). <https://doi.org:10.1557/mrs.2020.146>
- 13 Tisdale, J. T. *et al.* Precursor purity effects on solution-based growth of MAPbBr₃
single crystals towards efficient radiation sensing. *CrystEngComm* **20**, 7818-7825
(2018). <https://doi.org:10.1039/C8CE01498A>
- 14 Amari, S., Verilhac, J.-M., Gros D'Aillon, E., Ibanez, A. & Zaccaro, J.
Optimization of the Growth Conditions for High Quality CH₃NH₃PbBr₃ Hybrid
Perovskite Single Crystals. *Crystal Growth & Design* **20**, 1665-1672 (2020).
<https://doi.org:10.1021/acs.cgd.9b01429>
- 15 Kumar, S., Rukban, A., Sinisi, J., Damle, V. H. & Cahen, D. Localized Heating
Tailors Nucleation for Reproducible Growth of Thin Halide Perovskite Single
Crystals. *Crystal Growth & Design* **22**, 7160-7167 (2022).
<https://doi.org:10.1021/acs.cgd.2c00833>
- 16 Sebastian, V. Toward continuous production of high-quality nanomaterials using
microfluidics: nanoengineering the shape, structure and chemical composition.
Nanoscale **14**, 4411-4447 (2022). <https://doi.org:10.1039/D1NR06342A>
- 17 Iglesias, D., Haddad, D. & Sans, V. Recent Developments in Process
Digitalisation for Advanced Nanomaterial Syntheses. *Chemistry-Methods* **2**
(2022). <https://doi.org:10.1002/cmtd.202200031>
- 18 Das Adhikari, S. *et al.* Continuous-Flow Synthesis of Orange Emitting Sn(II)-
Doped CsBr Materials. *Advanced Optical Materials* **9**, 2101024 (2021).
<https://doi.org:https://doi.org/10.1002/adom.202101024>
- 19 Iglesias, D. *et al.* 3D printed flow reactors for the synthesis of single crystal
perovskites. *Materials Today Energy* **39**, 101476 (2024).
<https://doi.org:https://doi.org/10.1016/j.mtener.2023.101476>
- 20 Epps, R. W. *et al.* Artificial Chemist: An Autonomous Quantum Dot Synthesis
Bot. *Advanced Materials* **32**, 2001626 (2020).
<https://doi.org:https://doi.org/10.1002/adma.202001626>
- 21 Savage, T. *et al.* Machine learning-assisted discovery of flow reactor designs.
Nature Chemical Engineering **1**, 522-531 (2024). <https://doi.org:10.1038/s44286-024-00099-1>
- 22 Lee, C.-Y., Wang, W.-T., Liu, C.-C. & Fu, L.-M. Passive mixers in microfluidic
systems: A review. *Chemical Engineering Journal* **288**, 146-160 (2016).
<https://doi.org:https://doi.org/10.1016/j.cej.2015.10.122>
- 23 Bettermann, S., Kandelhard, F., Moritz, H.-U. & Pauer, W. Digital and lean
development method for 3D-printed reactors based on CAD modeling and CFD

- simulation. *Chemical Engineering Research and Design* **152**, 71-84 (2019).
<https://doi.org/10.1016/j.cherd.2019.09.024>
- 24 Gonzalez, G., Roppolo, I., Pirri, C. F. & Chiappone, A. Current and emerging trends in polymeric 3D printed microfluidic devices. *Additive Manufacturing* **55**, 102867 (2022). <https://doi.org/10.1016/j.addma.2022.102867>
- 25 Parra-Cabrera, C., Achille, C., Kuhn, S. & Ameloot, R. 3D printing in chemical engineering and catalytic technology: structured catalysts, mixers and reactors. *Chemical Society Reviews* **47**, 209-230 (2018).
<https://doi.org/10.1039/C7CS00631D>
- 26 Yue, J., Falke, F. H., Schouten, J. C. & Nijhuis, T. A. Microreactors with integrated UV/Vis spectroscopic detection for online process analysis under segmented flow. *Lab on a Chip* **13**, 4855-4863 (2013).
<https://doi.org/10.1039/C3LC50876E>
- 27 Epps, R. W., Felton, K. C., Coley, C. W. & Abolhasani, M. Automated microfluidic platform for systematic studies of colloidal perovskite nanocrystals: towards continuous nano-manufacturing. *Lab on a Chip* **17**, 4040-4047 (2017).
<https://doi.org/10.1039/C7LC00884H>
- 28 Pinho, B. & Torrente-Murciano, L. Dial-A-Particle: Precise Manufacturing of Plasmonic Nanoparticles Based on Early Growth Information—Redefining Automation for Slow Material Synthesis. *Advanced Energy Materials* **11**, 2100918 (2021). <https://doi.org/10.1002/aenm.202100918>
- 29 Bateni, F. *et al.* Smart Dope: A Self-Driving Fluidic Lab for Accelerated Development of Doped Perovskite Quantum Dots. *Advanced Energy Materials* **14**, 2302303 (2024). <https://doi.org/10.1002/aenm.202302303>
- 30 Lignos, I., Maceiczky, R. M., Kovalenko, M. V. & Stavarakis, S. Tracking the Fluorescence Lifetimes of Cesium Lead Halide Perovskite Nanocrystals During Their Synthesis Using a Fully Automated Optofluidic Platform. *Chemistry of Materials* **32**, 27-37 (2020). <https://doi.org/10.1021/acs.chemmater.9b03438>
- 31 Okafor, O. *et al.* Advanced reactor engineering with 3D printing for the continuous-flow synthesis of silver nanoparticles. *Reaction Chemistry & Engineering* **2**, 129-136 (2017). <https://doi.org/10.1039/C6RE00210B>
- 32 Haruta, Y. *et al.* Reproducible high-quality perovskite single crystals by flux-regulated crystallization with a feedback loop. *Nature Synthesis* (2024).
<https://doi.org/10.1038/s44160-024-00576-8>
- 33 Salas, A., Zanatta, M., Sans, V. & Roppolo, I. Chemistry in light-induced 3D printing. *ChemTexts* **9**, 4 (2023). <https://doi.org/10.1007/s40828-022-00176-z>
- 34 Sans, V., Karbass, N., Burguete, M. I., García-Verdugo, E. & Luis, S. V. Residence time distribution, a simple tool to understand the behaviour of polymeric mini-flow reactors. *RSC Advances* **2**, 8721-8728 (2012).
<https://doi.org/10.1039/C2RA20903A>
- 35 *Open CV Library*, <www.opencv.org> (
36 Tinajero, C. *VCA Algorithm*, <<https://github.com/catm542-ai/PerovskiteGrowthDetection/blob/main/LICENSE>> (
37 Boopathi, K. M. *et al.* Permanent Lattice Compression of Lead-Halide Perovskite for Persistently Enhanced Optoelectronic Properties. *ACS Energy Letters* **5**, 642-649 (2020). <https://doi.org/10.1021/acsenerylett.9b02810>
- 38 Schötz, K. *et al.* Double peak emission in lead halide perovskites by self-absorption. *Journal of Materials Chemistry C* **8**, 2289-2300 (2020).
<https://doi.org/10.1039/C9TC06251C>

- 39 Ding, J., Lian, Z., Li, Y., Wang, S. & Yan, Q. The Role of Surface Defects in Photoluminescence and Decay Dynamics of High-Quality Perovskite MAPbI₃ Single Crystals. *The Journal of Physical Chemistry Letters* **9**, 4221-4226 (2018). <https://doi.org:10.1021/acs.jpcllett.8b01898>
- 40 Niemann, R. G. *et al.* Halogen Effects on Ordering and Bonding of CH₃NH₃⁺ in CH₃NH₃PbX₃ (X = Cl, Br, I) Hybrid Perovskites: A Vibrational Spectroscopic Study. *The Journal of Physical Chemistry C* **120**, 2509-2519 (2016). <https://doi.org:10.1021/acs.jpcc.5b11256>
- 41 Petrov, A. A., Ordinartsev, A. A., Fateev, S. A., Goodilin, E. A. & Tarasov, A. B. Solubility of Hybrid Halide Perovskites in DMF and DMSO. *Molecules* **26**, 7541 (2021).